Enhancement of the linear electro-optic effect by high pressure

Yuewen Gao,[1] Yu Gu,[1] Toshiaki Iitaka,[2] and Zhi Li[1,*]

[1]*MIIT Key Laboratory of Advanced Display Materials and Devices, School of Materials and Engineering, Nanjing University of Science and Technology, Nanjing 210094, China*

[2]*Discrete Event Simulation Research Team, RIKEN Center for Computational Science, 2-1 Hirosawa, Wako Saitama 351-0198, Japan*

(Received 28 February 2023; accepted 5 June 2023; published 20 June 2023)

It is challenging to design electro-optic (EO) crystals with both a large bandgap and a high EO coefficient. We propose that some semiconductors synthesized under a high pressure environment can present both a large bandgap and a high linear EO coefficient because of the enhanced strength of the valence bond. The electronic band structures and linear EO coefficients of the $II SiN_2$ (II = Mg, Sr, Ba) compounds are studied using first-principles calculation. Our calculated results predict that both $SrSiN_2$ and $BaSiN_2$, under a high-pressure condition, will crystalize into an orthorhombic structure with the same space group of $MgSiN_2$ under ambient pressure. The calculated bandgaps are 5.48, 4.41, and 3.57 eV, respectively, for $MgSiN_2$, $SrSiN_2$, and $BaSiN_2$, while the calculated linear EO coefficients are 1.55, 12.09, and 21.60 pm/V at a fiber communication wavelength of 1550 nm. The increasing linear EO coefficients can be interpreted by the enhanced bond strength and a reduced bandgap. This work indicates that it is feasible to enhance the linear EO coefficient with high pressure.

DOI: 10.1103/PhysRevB.107.245203

I. INTRODUCTION

The electro-optic modulator (EOM), which modulates the phase, frequency, amplitude, or polarization of light by low-frequency electric signals within the principle of the electro-optic (EO) effect, is one fundamental active device in integrated photonics applications, including intrachip data transmission [1–6], neuromorphic logic optical chips [7–11], and photonic integrated circuits for quantum computing [12–14]. The EO effect describes the change of the complex refractive index (CRI), $N = n + ik$ of materials in response to an electric field that varies slowly with time compared with the frequency of light. The real part of CRI, $n(\omega) = \sqrt{\frac{|\varepsilon|+\varepsilon_1}{2}}$, determines the phase velocity, while the imaginary part, $k = \sqrt{\frac{|\varepsilon|-\varepsilon_1}{2}}$, determines the optical attenuation of light propagating in the medium, where ε_1 (ε_2) is the real (imaginary) part of the frequency-dependent complex dielectric function $\varepsilon = \varepsilon_1 + i\varepsilon_2$. In practice, phase modulation is favored for high-speed and low-power optical devices; we usually adopt EO crystals with a relatively large bandgap and a relatively small attenuation coefficient k at working wavelengths, which usually is 1550 nm for fiberoptic communication. The linear electro-optic (LEO) effect, or Pockels effect [15–19], describes the change of the dielectric tensor $\varepsilon_{ij}(E)/\varepsilon_0 = \varepsilon_{ij}^{(1)} + \chi_{ijk}^{(2)}(\omega;\omega,0)E_k$, in which $\varepsilon_{ij}^{(1)}$ is the dielectric tensor within linear response theory and $\chi_{ijk}^{(2)}(\omega;\omega,0)$ is the LEO coefficient under a low-frequency electric signal E. The complex EO coefficient $\chi_{ijk}^{(2)}(\omega;\omega,0) = \alpha_{ijk} + i\beta_{ijk}$ [20] usually has a symmetric (antisymmetric) real (imaginary) part under exchange of indices j and k described the second-order response under an optical field with linear (circular) polarization. The real part results from the mechanism of the shift vector, which characterizes the position difference between the Wannier centers of the valance and conduction bands [21–24], while the imaginary part results from the curvature tensor associated with the band structure near the Fermi level [25]. In the case of a large bandgap, ε_{ij}(E) is real and optical absorption is neglectable, the real refractive index $n = n_0 \pm \frac{\chi^{(2)}E}{2n_0}$ for light with two orthogonal polarizations, in which n_0 is the real refractive index within linear response theory, i.e., the two polarized states have different phase velocities. For excellent EO crystals, a large EO coefficient is necessary for a relatively low half-wave voltage V_π. The semiconductor $LiNbO_3$ (LN), which has relatively large bandgap of 3.61 eV and a LEO coefficient of about 32 pm/V at an input wavelength of 1550 nm [26–28], is the main commercial EO crystal and is widely used for EOM devices. For semiconductors with a relatively small bandgap, larger EO coefficients are feasible, such as the $BaTiO_3$ crystal [29–32]. However, this enhancement of the EO coefficient is not meaningful because of the sacrifice of the bandgap. For the typical communication wavelength of 1550 nm (photon energy ~0.8 eV), resonant absorption can be safely prohibited in insulators with a larger bandgap; therefore, it will be more significant if we can enhance both the EO coefficient and bandgap simultaneously. It is challenging work to design novel EO crystals with both a large bandgap and EO coefficient. By growing the EO crystals on some substrates, the interface strain can improve the EO coefficient somewhat [26,33–36]. However, strain engineering cannot enhance the EO effect efficiently.

In this work, we start from the two-band model of a massive Weyl fermion [37] and predict a high LEO coefficient resulting from the enhancement of orbital hybridization under high pressure. Then, we take the silicon nitride (Si_3N_4)

*zhili@njust.edu.cn

 ©2023 American Physical Society

electron-optical crystal as a prototype, and replace one silicon atom by two alkaline-earth metal atoms and predict that both $SrSiN_2$ and $BaSiN_2$ under high pressure will crystalize into an orthorhombic structure with the space group $Pna2_1$ of $MgSiN_2$ under ambient pressure by the first-principles calculation. Further, we calculate the band structures and EO coefficients of isostructural $IISiN_2$ (II = Mg, Sr, Ba) to justify our proposal, viz., high pressure is an efficient approach to enhancing the LEO coefficient.

II. PRINCIPLE

From a simple, two-band effective Hamiltonian for a massive Weyl fermion

$$h_0(\vec{k}) = \begin{pmatrix} \Delta(k_z) & \lambda(k_x - ik_y) \\ \lambda(k_x + ik_y) & -\Delta(k_z) \end{pmatrix}, \tag{1}$$

in which positive 2Δ is the charge transfer energy (or fermion mass) and λ tunes the strength of orbital hybridization, which is an odd function of momentum because of the broken spatial inversion symmetry, the eigenvectors for the valence and conducting bands read $u_c = \begin{pmatrix} \cos\theta(\vec{k}) \\ \sin\theta(\vec{k})e^{i\varphi(\vec{k})} \end{pmatrix}$ and $u_v = \begin{pmatrix} \sin\theta(\vec{k})e^{-i\varphi(\vec{k})} \\ -\cos\theta(\vec{k}) \end{pmatrix}$, respectively, and $\cos\theta(\vec{k}) = \sqrt{\frac{d+\Delta}{2d}}$, $\sin\theta(\vec{k})e^{i\varphi(\vec{k})} = \frac{\lambda(k_x+ik_y)}{\sqrt{2d(d+\Delta)}}$, and $d(\vec{k}) = \sqrt{\Delta^2 + \lambda^2 k^2}$ [25]. For wide-bandgap insulators, the nonlinear optic response is dominated by the nonlinear polarization or current induced by the shift vector, which characterizes the position difference of the Wannier center between the conduction and valence bands [20]. We consider the shift vector induced the oscillating second-order current with frequency ω. Under an oscillating optical field $\vec{E}(\omega)$ with frequency ω and static electric field $\vec{E}_0$, within dipole approximation, the oscillating second-order current density with frequency ω reads [38]

$$\vec{j}(\omega;\omega,0) = -\frac{e}{\hbar}\frac{1}{(2\pi)^3}\int d\vec{k}\sum_{m\neq n}\rho^{(1)}_{nm}(\vec{k},\omega)\vec{D}_{mn} \times (\vec{k})\vec{E}_0 \cdot \vec{A}_{nm}(\vec{k}) \tag{2}$$

$$\rho^{(1)}_{nm}(\vec{k},\omega) = \frac{e\vec{E}(\omega)\cdot\vec{A}_{mn}(\vec{k})}{\hbar(\omega - i\eta) - \varepsilon_{mn}(\vec{k})}\left[\rho^{(0)}_{mm}(\vec{k}) - \rho^{(0)}_{nn}(\vec{k})\right], \tag{3}$$

where the shift vector $\vec{D}_{mn}(\vec{k}) = \partial_{\vec{k}} + i\vec{A}_{mm}(\vec{k}) - i\vec{A}_{nn}(\vec{k})$ is gauge invariant and characterizes the position difference of the Wannier centers, $\vec{A}_{nm}(\vec{k})$ is the Berry connection and is gauge dependent, and $\varepsilon_{mn}(\vec{k}) = \varepsilon_m(\vec{k}) - \varepsilon_n(\vec{k})$ is the energy difference between the Bloch bands m and n with the initial Fermi-Dirac distribution $\rho^{(0)}_{mm}(\vec{k})$ and $\rho^{(0)}_{nn}(\vec{k})$, respectively. The summation in Eq. (2) is performed on all band indices except $m = n$, and the interband density matrix $\rho^{(1)}_{nm}(\vec{k},\omega)$ in Eq. (3) is proportional to the strength of the optical field. Since the current $\vec{j}(\omega;\omega,0)$ is gauge invariant under any local phase transformation of Bloch functions, we only focus on the amplitudes of the density matrix and the Berry connection. With a simple two-band model for a massive Weyl fermion in Eq. (1), i.e., one valence and one conduction band, $\Delta(k_z)$ takes a minimum at the topmost point of valence band $\vec{k}_w = (0,0,k_w)$, and the calculated interband Berry connection $|\vec{A}_{cv}(\vec{k}_w)| \sim \frac{\lambda}{2\Delta}$ is proportional to the parameter λ [25], and is inversely proportional to the bandgap $2\Delta(k_w)$. Therefore, the amplitude of the first-order density matrix $|\rho^{(1)}_{cv}(0,\omega)| \propto \frac{\lambda}{\Delta^2}$ if the photon energy is much lower than the bandgap. With a proper phase gauge, the shift vector $|\vec{D}_{mn}(\vec{k})| \propto \frac{\lambda^2}{\Delta}$. Because the amplitude of the Berry connection $|\vec{A}_{vc}(0)| \propto \frac{\lambda}{\Delta}$ near the Weyl point $(0,0,k_w)$ and the second-order susceptibility, $\chi^{(2)}(\omega;\omega,0) = \vec{P}(\omega;\omega,0)/|\vec{E}_0||\vec{E}(\omega)|$ is approximately proportional to $(\frac{\lambda}{\Delta})^4$, where $E_g = 2\Delta(\vec{k}_w)$ is the bandgap. This result indicates that strong orbital hybridization can enhance the LEO coefficient while the wide bandgap is maintained. With the increase of parameter λ, the slope of band dispersion $\varepsilon(\vec{k}) = \pm d(\vec{k})$ around the bandgap will increase. The slope of band dispersion also characterizes the bond strength. It is well known that high pressure can compress lattice parameters and enhance orbital hybridization [39–41]. Therefore, it should be feasible to enhance the LEO coefficient by high pressure, which renders a relatively short bond length and a strong valance bond strength.

III. MATERIAL CANDIDATES

Silicon nitride is an insulator with a bandgap of about 4.78 eV [42] and a relatively low LEO coefficient of about 15 pm/V [43]. However, the high-pressure phases of Si_3N_4 are centrosymmetric [44–46], and the LEO effect is vanishing. Therefore, we replace one silicon atom by two alkaline-earth metal atoms, and the equations of state (EOS) of $IISiN_2$ (II = Mg, Sr, Ba) compounds are calculated by the first-principles calculation based on density functional theory with the Perdew-Burke-Ernzerhof (PBE) exchange-correlation functional [47] implemented in the Vienna Ab initio Simulation Package [48] code with an energy cut of 500 eV and $13 \times 13 \times 10$ k-points sampling, as shown in Supplemental Material Fig. S1 (left) [49]. At ambient pressure, $MgSiN_2$ crystalizes into an orthogonal structure with space group $Pna2_1$ [50,51], while $SrSiN_2$ and $BaSiN_2$ crystalize into a monoclinic structure with space group $P2_1c$ [52] and an orthogonal structure with space group $Cmca$ [52], respectively. Both $SrSiN_2$ with space group $P2_1c$ and $BaSiN_2$ with space group $Cmca$ are centrosymmetric materials; therefore, neither of them has a LEO effect. Therefore, we replace the magnesium atoms in $MgSiN_2$ by strontium atoms and barium atoms to form $SrSiN_2$ and $BaSiN_2$, respectively, with the space group $Pna2_1$ (No. 33) [the crystal structure of $IISiN_2$ (II = Mg, Sr, Ba) is shown in Supplemental Material Fig. S1 (right) [49]] and compare the structural stability of $SrSiN_2$ ($BaSiN_2$) with the $Pna2_1$ and $P2_1c$ ($Cmca$) space groups by the total energy calculation with a different volume of unit cells. The calculated EOS of $SrSiN_2$ and $BaSiN_2$ is shown in Fig. 1, which demonstrates that both $SrSiN_2$ and $BaSiN_2$ can crystalize into the $Pna2_1$ space group under high pressure.

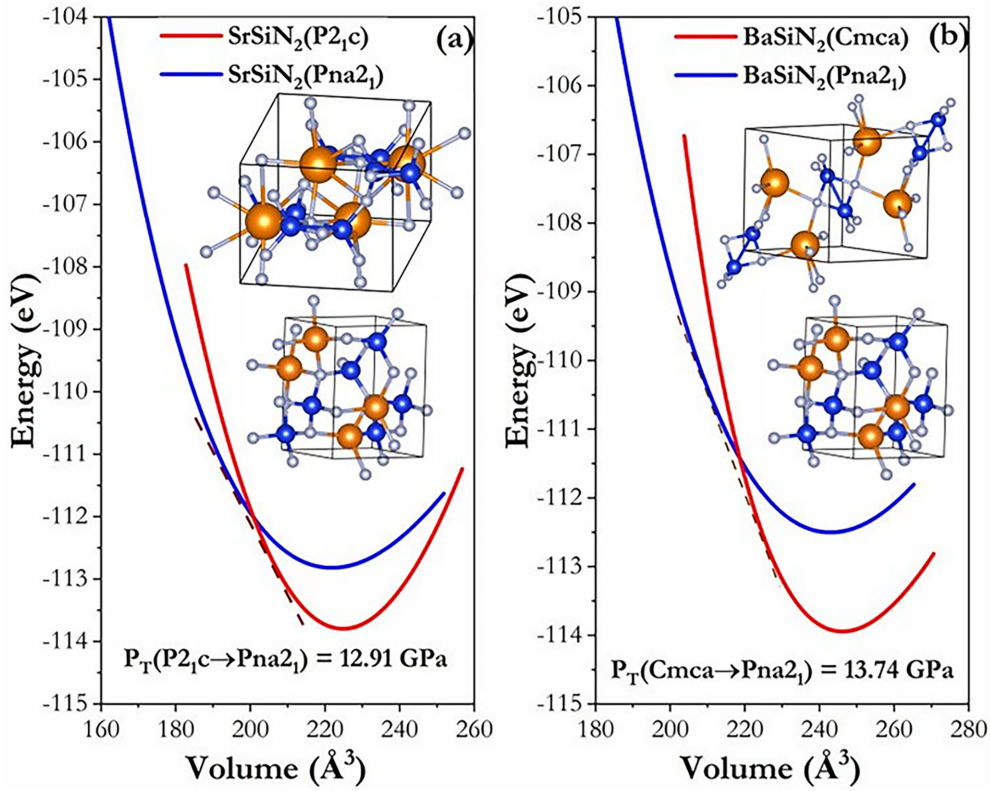

FIG. 1. Both $SrSiN_2$ and $BaSiN_2$ will crystalize into an orthorhombic structure with space group $Pna2_1$ under high pressure, and the phase transition pressure is determined to be 12.91 and 13.74 GPa, respectively. (a) Calculated EOS of $SrSiN_2$ with space groups $Pna2_1$ and $P2_1c$, where the inset shows the crystal structure of the space group $P2_1c$ and $Pna2_1$, respectively. Strontium, silicon, and nitrogen atoms are shown as bronze, blue, and gray spheres respectively. (b) EOS of $BaSiN_2$ with space groups $Pna2_1$ and $Cmca$, where the inset shows the crystal structure of the space group $Cmca$ and $Pna2_1$, respectively. Barium, silicon, and nitrogen atoms are shown as bronze, blue, and gray spheres, respectively.

The calculated pressure of this phase transition is about 12.91 and 13.74 GPa for $SrSiN_2$ and $BaSiN_2$, respectively. The orthorhombic $IISiN_2$ compounds with space group $Pna2_1$ are noncentrosymmetric crystals with a nonvanishing LEO effect, and they afford an excellent platform to study the LEO effect of crystals synthesized under a high-pressure environment.

IV. ELECTRONIC STRUCTURES AND LINEAR OPTICAL PROPERTIES

After the phase transition under high pressure is confirmed by the total energy calculations, the electronic structure and linear optical properties are calculated by an all-electron, full-potential linearized augmented plane wave implemented in ELK code [53] with energy cut $R_{MT} \times K_{max} = 7.0$ and $13 \times 13 \times 10$ k-points sampling. The muffin-tin radius R_{MT} reads 2.2, 2.6, and 2.8 a.u. for magnesium, strontium, and barium, respectively. The optimized structural parameters of $IISiN_2$ (II = Mg, Sr, Ba) are tabulated in Supplemental Material Table SI [49]. Since there is no heavy element, the spin-orbital coupling (SOC) effect is very weak in the noncentrosymmetric material $MgSiN_2$ compound, as shown in Supplemental Material Fig. S2 [49]. Therefore, we ignored the SOC effect in the first-principles calculation. We also ignored the exciton effect, because the exciton binding energy is usually very low in the bulk of our proposed materials [50,54]. The calculated band structure of orthogonal $MgSiN_2$ with space group $Pna2_1$ by the PBE exchange-correlation functional is shown in Supplemental Material Fig. S2(a) [49], and the calculated bandgap is 3.93 eV, which is seriously underestimated, in contrast to the experimental value 5.62 eV by de Boer *et al.* [55]. The calculated band structure of $MgSiN_2$ with space group $Pna2_1$ obtained with the modified Becke-Johnson (MBJ) approximation [56] is shown in Fig. 2(a), and the calculated bandgap of 5.48 eV is consistent with the experimental value [55]. The economical MBJ approximation can also afford relatively accurate bandgaps for insulators and good agreement with hybrid functions or the GW method [57]. The calculated band structures of $SrSiN_2$ and $BaSiN_2$ with space group $Pna2_1$ with MBJ approximation are shown in Fig. 2(b) and 2(c), respectively. The calculated bandgaps of $SrSiN_2$ and $BaSiN_2$ are 4.41 eV and 3.57 eV, respectively, and the weight of s orbitals from alkaline-earth metal atoms (silicon and nitrogen atoms) are marked by red circles. The calculated partial density of states (PDOS) of $MgSiN_2$, $SrSiN_2$, and $BaSiN_2$ with space group $Pna2_1$ obtained within MBJ approximation is shown in Fig. 2(d)–2(f). The calculated electronic structures show that p orbitals of the silicon/nitrogen elements dominate the top of the valance band, while the s orbitals from alkaline-earth metal element dominates the bottom of the conduction bands in all $IISiN_2$ (II = Mg, Sr, Ba) compounds. Our calculated results

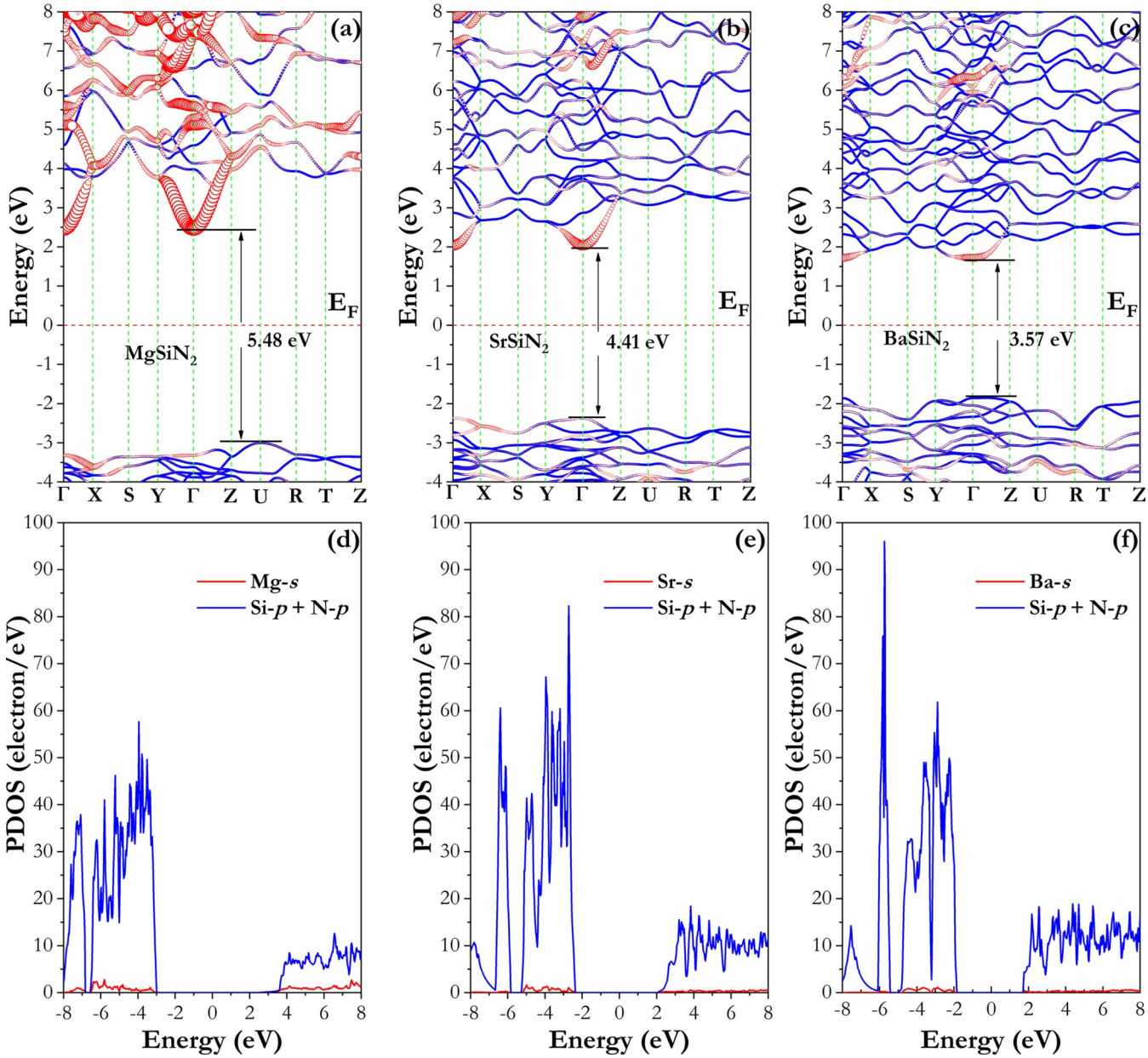

FIG. 2. Band structures of $MgSiN_2$ (a), $SrSiN_2$ (b), and $BaSiN_2$ (c) with space group $Pna2_1$ by the first-principles calculation within the MBJ approximation. The calculated PDOS of $MgSiN_2$ (d), $SrSiN_2$ (e), and $BaSiN_2$ (f) with space group $Pna2_1$ is obtained using the MBJ approximation. The PDOS of the magnesium, strontium, barium, silicon, and nitrogen atoms are shown, as well as the projection onto the *s* orbital (red) of the alkaline-earth metal atomic species and the *p* orbitals (blue) of the silicon/nitrogen atomic species.

demonstrate that the bandgap of $II SiN_2$ (II = Mg, Sr, Ba) compounds becomes smaller with the increasing atomic mass of alkaline-earth metals, and the reduced bandgap can be interpreted by a reduced charge transfer energy between *s* orbitals of alkaline-earth metals and *p* orbitals of silicon/nitrogen elements with the increase in mass of alkaline-earth metals. In the band structure of $SrSiN_2$, obvious *sp* hybridization occurs at the Γ(0,0,0) point, as shown in Fig. 2(b), and presents the character of a massive Weyl fermion and strong bond strength.

Within linear response theory, linear optical properties (including both interband and intraband contributions) are also calculated by ELK code with same computational details as the band structure. The calculated dielectric function $\varepsilon(\omega)$ of $MgSiN_2$, $SrSiN_2$, and $BaSiN_2$ is shown in Supplemental Material Fig. S3 [49], and the real part of CRI $n(\omega)$ and the imaginary part of CRI $k(\omega)$ of $MgSiN_2$, $SrSiN_2$, and $BaSiN_2$ are shown in Fig. 3(a) and 3(b), respectively. With the atomic mass of the alkaline-earth metal increases in the $II SiN_2$ compounds, both the calculated refractivity $n_{xx}(\omega)$ and the extinction coefficient (or attenuation index) $k_{xx}(\omega)$ increase gradually with the low frequency of incident photons before resonant absorption. The calculated refractivity $n_{xx}(\omega)$ of $MgSiN_2$, $SrSiN_2$, and $BaSiN_2$ at the static limit are about 1.84, 2.00, and 2.28, and the refractivity of $BaSiN_2$ is larger than that of LN [15]. Additionally, the extinction

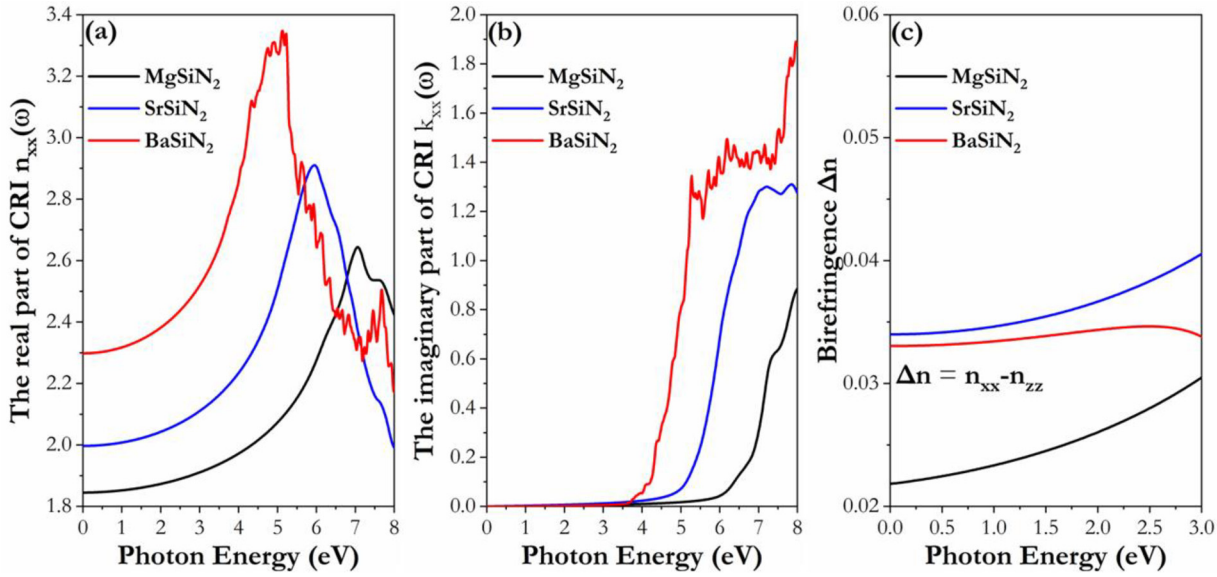

FIG. 3. The real part of CRI $n(\omega)$ (a), the imaginary part of CRI $k(\omega)$ (b), and the calculated photon energy-dependent birefringence (c) of $II\mathrm{SiN_2}$ (II = Mg, Sr, Ba) with space group $Pna2_1$ by the first-principles calculation.

coefficient (or attenuation index) $k_{xx}(\omega)$ is almost zero, with the low frequency of incident photons indicating neglectable absorption and attenuation when the light, with wavelength 1550 nm, propagates through the $II\mathrm{SiN_2}$ compounds.

Moderate birefringence $\Delta n = n_{xx} - n_{zz}$ is another criterion for an excellent nonlinear optical crystal. At the static limit, both $\mathrm{MgSiN_2}$ and $\mathrm{BaSiN_2}$ present a relatively small birefringence, as shown in Fig. 3(c), and $\mathrm{SrSiN_2}$ presents a relatively large birefringence. The calculated birefringence of $\mathrm{SrSiN_2}$ at an input wavelength of 1550 nm is about 0.034, which is smaller than that of LN [15]. The calculated birefringence of both $\mathrm{MgSiN_2}$ and $\mathrm{SrSiN_2}$ increases with the increase in frequency of incident photons, while $\mathrm{BaSiN_2}$ has a peak at an input wavelength of about 500 nm.

V. THE LEO COEFFICIENT

The LEO coefficient contributed by the shift vector mechanism is calculated by the first principles calculation code ABINIT [58] within the sum-over-state approximation [59]. The scissor operator is determined to be the energy difference between the MBJ and PBE bandgap, and k-points sampling is set to be 26 × 26 × 20. Because of the mm2 point group, there are seven nonvanishing elements. The calculated element $\chi^{(2)}_{xyz}(\omega;\omega,0)$ is dominating, in contrast to the other elements. The calculated frequency-dependent LEO coefficient $\chi^{(2)}_{xyz}(\omega;\omega,0)$ of the $\mathrm{MgSiN_2}$, $\mathrm{SrSiN_2}$, and $\mathrm{BaSiN_2}$ compounds is shown in Fig. 4(a). In the energy range of 0 to 2.0 eV, the LEO coefficient of the $II\mathrm{SiN_2}$ (II = Mg, Sr, Ba) compounds increases with the increase of photon energy, while the imaginary parts of the LEO coefficient of the $II\mathrm{SiN_2}$ (II = Mg, Sr, Ba) compounds are neglectable in the energy range of 0 to 2.0 eV. The calculated LEO coefficients of $\mathrm{MgSiN_2}$, $\mathrm{SrSiN_2}$, and $\mathrm{BaSiN_2}$ are 1.55, 12.09, and 21.60 pm/V at a fiber-optic communication wavelength of 1550 nm. Both $\mathrm{SrSiN_2}$ and $\mathrm{BaSiN_2}$ synthesized under a high-pressure condition present a much higher LEO coefficient, while the LEO coefficient of $\mathrm{MgSiN_2}$ is very low. We define parameter $\Lambda = \chi^{(2)}_{xyz}(\omega;\omega,0) \times E_g$, which is the product of the bandgap and LEO coefficient at 1550 nm. As shown in Fig. 4(b), the parameter Λ increases rapidly with the decrease in bandgap in the $II\mathrm{SiN_2}$ (II = Mg, Sr, Ba) compounds. In contrast, the typical semiconductor $\mathrm{Si_3N_4}$ ($\mathrm{LiNbO_3}$) has a bandgap of 4.78 eV (3.61 eV) and a LEO coefficient of 15 pm/V (32 pm/V) at a wavelength of 1550 nm [15,42,43]. As typical EO crystals, both $\mathrm{Si_3N_4}$ and $\mathrm{LiNbO_3}$ present relatively high Λ. Additionally, both $\mathrm{SrSiN_2}$ and $\mathrm{BaSiN_2}$ have a larger quantity $\chi^{(2)}_{xyz}(\omega;\omega,0) \times (E_g)^4$ than that of $\mathrm{MgSiN_2}$. From our previous analysis, the LEO coefficient $\chi^{(2)}_{xyz}(\omega;\omega,0)$ should be proportional to $(\lambda/E_g)^4$. For both $\mathrm{SrSiN_2}$ and $\mathrm{BaSiN_2}$, the relatively large quantity $\chi^{(2)}_{xyz}(\omega;\omega,0) \times (E_g)^4$ can be interpreted by the increase in bond strength λ, which is enhanced by the high pressure. Although the $II\mathrm{SiN_2}$ (II = Mg, Sr, Ba) compounds have a relatively lower LEO coefficient than that of $\mathrm{LiNbO_3}$, our calculated results validated that the LEO coefficient is not determined by the bandgap exclusively, and it is feasible to enhance the LEO coefficient by high pressure, while the large bandgap is maintained or slightly reduced. The bandgap, LEO coefficient, and birefringence Δn of

TABLE I. The bandgap, LEO coefficient, and birefringence Δn of $II\mathrm{SiN_2}$ (II = Mg, Sr, Ba) compounds with space group $Pna2_1$, $\mathrm{Si_3N_4}$, and LN obtained by the first-principles calculation.

Compound	Bandgap (eV)	LEO coefficient (pm/V) at 1550 nm	Δn (static)	Reference
$\mathrm{MgSiN_2}$	5.48	1.55	0.023	[a]
$\mathrm{SrSiN_2}$	4.41	12.09	0.034	[a]
$\mathrm{BaSiN_2}$	3.57	21.60	0.033	[a]
$\mathrm{Si_3N_4}$	4.78	15	0.022	[31,37]
$\mathrm{LiNbO_3}$	3.61	32	0.073	[25,27,28]

[a]Current work.

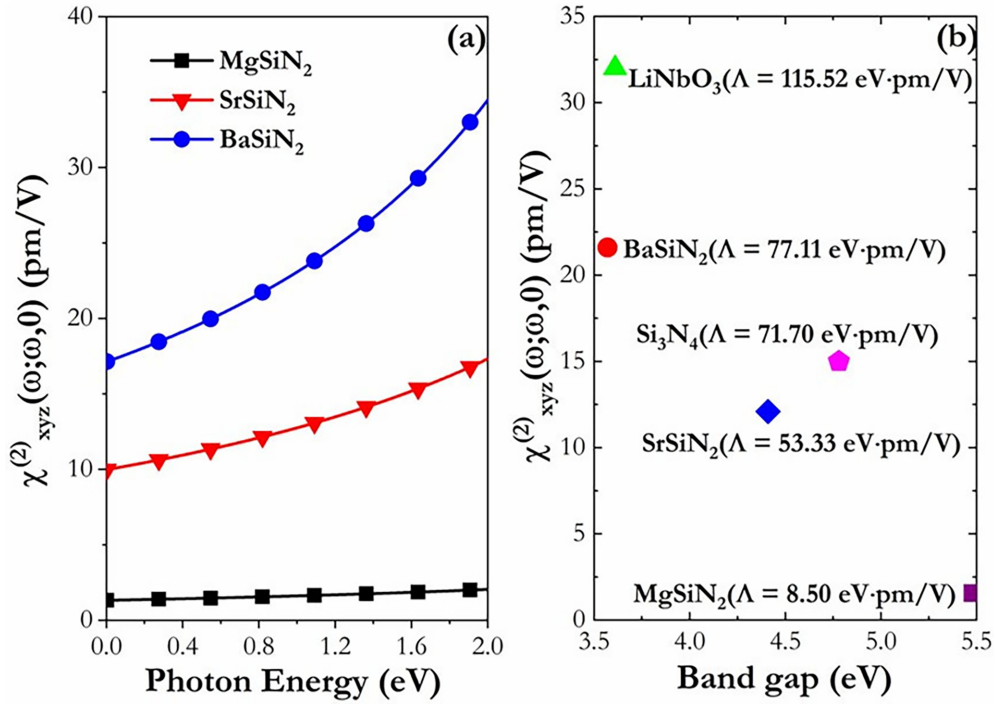

FIG. 4. (a) Calculated frequency-dependent LEO coefficient $\chi^{(2)}_{xyz}(\omega;\omega,0)$ of $MgSiN_2$, $SrSiN_2$, and $BaSiN_2$ with space group $Pna2_1$ contributed by the shift vector mechanism, where $MgSiN_2$, $SrSiN_2$, and $BaSiN_2$ are represented by black squares, red triangles, and blue circles, respectively. (b) The relationship between the bandgap and LEO $\chi^{(2)}_{xyz}(\omega;\omega,0)$ at an input wavelength of 1550 nm of $MgSiN_2$, $SrSiN_2$, $BaSiN_2$, Si_3N_4, and LN, where $\Lambda = \chi^{(2)}_{xyz}(\omega;\omega,0) \times E_g$.

$II SiN_2$ (II = Mg, Sr, Ba) compounds, Si_3N_4, and $LiNbO_3$ are shown in Table I.

Last, it is necessary to determine the half-wave voltage of the $II SiN_2$ (II = Mg, Sr, Ba) EO crystal. There are two types of EOM, i.e., longitudinal modulation and transverse modulation. The half-wave voltage working at longitudinal modulation is given by $V_\pi = \frac{\lambda}{2n_e^3 r_{63}}$, where $\lambda = 1550$ nm, and the half-wave voltages of $SrSiN_2$ and $BaSiN_2$ are 8.01 kV and 2.91 kV, respectively. The half-wave voltage working at transverse modulation is given by $V_\pi = \frac{\lambda d}{n_e^3 r_{33} L}$ [60], adopting the same Mach-Zehnder structure as the $LiNbO_3$ EOM [61]. With parameters $\lambda = 1550$ nm, $d = 10$ μm, and $L = 8$ mm, and the half-wave voltage of $SrSiN_2$ and $BaSiN_2$ are 20.03 V and 7.28 V, respectively. The half-wave voltage of $SrSiN_2$ and $BaSiN_2$ is larger than that of $LiNbO_3$ (6.05 V) [60].

VI. CONCLUSION

From the theoretical analysis of a nonlinear optical response within the shift vector mechanism, we conclude that orbital hybridization or bond strength can also affect the LEO coefficient. First-principles calculations reveal that both $SrSiN_2$ and $BaSiN_2$ under a high-pressure condition will crystalize into an orthorhombic structure with the same space group $Pna2_1$ of $MgSiN_2$ under ambient pressure. For $II SiN_2$ (II = Mg, Sr, Ba) compounds, the bandgap decreases with the increase of atomic mass of alkaline-earth metals, and the LEO coefficient increases. The product of the second-order susceptibility $\chi^{(2)}_{xyz}(\omega;\omega,0)$ and bandgap indicates that the increase of the LEO coefficient is not exclusively determined by the reduced bandgap, and the enhanced bond strength is also of critical importance. Our calculated results justified our design principle, viz., high pressure can enhance the bond strength and the LEO coefficient. This work is significant for the design of excellent EO crystals with both a large bandgap and LEO coefficient.

ACKNOWLEDGMENTS

Y. Gu is supported by the Natural Science Foundation of Jiangsu Province (Grant No. BK20200071). This work used the computational resources of the Hokusai system provided by Riken Information System Division.

[1] S. Datta and B. Das, Electronic analog of the electro-optic modulator, Appl. Phys. Lett. **56**, 665 (1990).
[2] P. Kolchin, C. Belthangady, S. Du, G. Y. Yin, and S. E. Harris, Electro-Optic Modulator of Single Photons, Phys. Rev. Lett. **101**, 103601 (2008).
[3] M. Liu, X. Yin, E. Ulin-Avila, B. Geng, T. Zentgraf, L. Ju, F. Wang, and X. Zhang, A graphene-based broadband optical modulator, Nature (London) **474**, 64 (2011).
[4] G. T. Reed, G. Mashanovich, F. Y. Gardes, and D. J. Thomson, Silicon optical modulators, Nat. Photonics **4**, 518 (2010).

[5] G. Sinatkas, T. Christopoulos, O. Tsilipakos, and E. E. Kriezis, Electro-optic modulation in integrated photonics, J. Appl. Phys. **130**, 010901 (2021).

[6] Q. F. Xu, B. Schmidt, S. Pradhan, and M. Lipson, Micrometre-scale silicon electro-optic modulator, Nature (London) **435**, 325 (2005).

[7] B. Dong, J.-D. Chen, F.-Y. Lin, J. C. Norman, J. E. Bowers, and F. Grillot, Dynamic and nonlinear properties of epitaxial quantum-dot lasers on silicon operating under long- and short-cavity feedback conditions for photonic integrated circuits, Phys. Rev. A **103**, 033509 (2021).

[8] D. Markovic, A. Mizrahi, D. Querlioz, and J. Grollier, Physics for neuromorphic computing, Nat. Rev. Phys. **2**, 499 (2020).

[9] F. Murphy-Armando, M. Brehm, P. Steindl, M. T. Lusk, T. Fromherz, K. Schwarz, and P. Blaha, Light emission from direct band gap germanium containing split-interstitial defects, Phys. Rev. B **103**, 085310 (2021).

[10] B. J. Shastri, A. N. Tait, T. F. de Lima, W. H. P. Pernice, H. Bhaskaran, C. D. Wright, and P. R. Prucnal, Photonics for artificial intelligence and neuromorphic computing, Nat. Photonics **15**, 102 (2021).

[11] R. A. Soref and B. R. Bennett, Electrooptical effects in silicon, IEEE J. Quantum Electron. **23**, 123 (1987).

[12] T. D. Ladd, F. Jelezko, R. Laflamme, Y. Nakamura, C. Monroe, and J. L. O'Brien, Quantum computers, Nature (London) **464**, 45 (2010).

[13] J. L. O'Brien, A. Furusawa, and J. Vuckovic, Photonic quantum technologies, Nat. Photonics **3**, 687 (2009).

[14] E. Pelucchi, G. Fagas, I. Aharonovich, D. Englund, E. Figueroa, Q. Gong, H. Hannes, J. Liu, C.- Y. Lu, N. Matsuda, J.- W. Pan, F. Schreck, F. Sciarrino, C. Silberhorn, J. Wang, and K. D. Jöns, The potential and global outlook of integrated photonics for quantum technologies, Nat. Rev. Phys. **4**, 194 (2021).

[15] R. W. Boyd, *Nonlinear Optics*, 3rd ed. (Elsevier, New York, 2008).

[16] S. Abel, F. Eltes, J. E. Ortmann, A. Messner, P. Castera, T. Wagner, D. Urbonas, A. Rosa, A. M. Gutierrez, D. Tulli, P. Ma, B. Baeuerle, A. Josten, W. Heni, D. Caimi, A. A. Demkov, L. Czornomaz, J. Leuthold, P. Sanchis, and J. Fompeyrine, Large Pockels effect in micro- and nanostructured barium titanate integrated silicon, Nat. Mater. **18**, 42 (2019).

[17] M. Li and H. X. Tang, Strong Pockels materials, Nat. Mater. **18**, 9 (2019).

[18] Z. Sobiesierski, D. I. Westwood, and M. Elliott, Reflectance anisotropy spectra from Si δ-doped GaAs(001): Correlation of linear electro-optic effect with integrated surface field, Phys. Rev. B **56**, 15277 (1997).

[19] W. Wei and Z. D. Wang, Internal-noise-enhanced signal transduction in neuronal systems, Phys. Rev. E **55**, 7379 (1997).

[20] Z. Li, Y. Gao, Y. Gu, S. Zhang, T. Iitaka, and W. M. Liu, Berry curvature induced linear electro-optic effect in chiral semimetals, Phys. Rev. B **105**, 125201 (2022).

[21] J. Ahn, G.-Y. Guo, and N. Nagaosa, Low-Frequency Divergence and Quantum Geometry of the Bulk Photovoltaic Effect in Topological Semimetals, Phys. Rev. X **10**, 041041 (2020).

[22] C. Qian, C. Yu, S. Jiang, T. Zhang, J. Gao, S. Shi, H. Pi, H. Weng, and R. Lu, Role of Shift Current in High-Harmonic Generation Form Noncentrosymmetric Topological Insulator Under Strong Lasers Fields, Phys. Rev. X **12**, 021030 (2022).

[23] J. E. Sipe and A. I. Shkrebtii, Second-order optical response in semiconductors, Phys. Rev. B **61**, 5337 (2000).

[24] T. Morimoto and N. Nagaosa, Topological nature of nonlinear optical effects in solids, Sci. Adv. **2**, e1501524 (2016).

[25] Z. Li, S. Zhang, T. Tohyama, X. Song, Y. Gu, T. Iitaka, H. Su, and H. Zeng, Optical detection of quantum geometric tensors in intrinsic semiconductors, Sci. China Ser. G Phys. Mech. Astron. **64**, 107211 (2021).

[26] A. K. Hamze, M. Reynaud, J. Geler-Kremer, and A. A. Demkov, Design rules for strong electro-optic materials, npj Comput. Mater. **6**, 130 (2020).

[27] M. Li, J. Ling, Y. He, U. A. Javid, S. Xue, and Q. Lin, Lithium niobate photonic-crystal electro-optic modulator, Nat. Commun. **11**, 4123 (2020).

[28] C. Wang, M. Zhang, X. Chen, M. Bertrand, A. Shams-Ansari, S. Chandrasekhar, P. Winzer, and M. Lončа, Integrated lithium niobate electro-optic modulators operating at CMOS-compatible voltages, Nature (London) **562**, 101 (2018).

[29] F. Eltes, C. Mai, D. Caimi, Y. Popoff, G. Winzer, D. Petousi, S. Lischke, J. E. Ortmannn, L. Czornomaz, L. Zimmermann, J. Fompeyrine, and S. Abel, A $BaTiO_3$-based electro-optic Pockels modulator monolithically integrated on an advanced silicon photonics platform, J. Lightwave Tech. **37**, 1456 (2019).

[30] D. Sando, P. Hermet, J. Allibe, J. Bourderionnet, S. Fusil, C. Carrétéro, E. Jacquet, J.- C. Mage, D. Dolfi, A. Barthélémy, Ph. Ghose, and M. Bibes, Linear electro-optic effect in multiferroic $BiFeO_3$ thin films, Phys. Rev. B **89**, 195106 (2014).

[31] C. Xiong, W. H. P. Pernice, J. H. Ngai, J. W. Reiner, D. Kumah, F. J. Walker, C. H. Ahn, and H. X. Tang, Active silicon integrated nanophotonics: Ferroelectric $BaTiO_3$ devices, Nano Lett. **14**, 1419 (2014).

[32] M. Zgonik, P. Bernasconi, M. Duelli, R. Schlessnar, P. Günter, M. H. Garrett, D. Rytz, Y. Zhu, and X. Mu, Dielectric, elastic, piezoelectric, electro-optic, and elastro-optic tensors of $BaTiO_3$ crystals, Phys. Rev. B **50**, 5941 (1994).

[33] C. Ederer and N. A. Spaldin, Effect of Epitaxial Strain on the Spontaneous Polarization of Thin Film Ferroelectrics, Phys. Rev. Lett. **95**, 257601 (2005).

[34] M. N. Valdez, H. T. Spanke, and N. A. Spaldin, *Ab initio* study of the ferroelectric strain dependence and 180 ° domain walls in the barium metal fluorides $BaMgF_4$ and $BaZnF_4$, Phys. Rev. B **93**, 064112 (2016).

[35] S. Kondo, T. Yamada, A. K. Tagantsev, P. Ma, J. Leuthold, P. Martelli, M. Martinslli, P. Boffi, M. Yoshino, and T. Nagasaki, Large impact of strain on the electro-optic effect in (Ba, Sr)TiO_3 thin films: Experiment and theoretical comparison, Appl. Phys. Lett. **115**, 092901 (2019).

[36] C. Paillard, S. Prokhorenko, and L. Bellaiche, Strain engineering of electro-optic constants in ferroelectric materials, npj Comput. Mater. **5**, 6 (2019).

[37] B. Q. Lv, T. Qian, and H. Ding, Experimental perspective on three-dimensional topological semimetals, Rev. Mod. Phys. **93**, 025002 (2021).

[38] H. Rostami and M. Polini, Nonlinear anomalous photocurrents in Weyl semimetals, Phys. Rev. B **97**, 195151 (2018).

[39] Z. Li, Q. Liu, Y. Wang, T. Iitaka, H. Su, T. Tohyama, Z. Yang, and S. Pan, Second-harmonic generation in

noncentrosymmetric phosphates, Phys. Rev. B **96**, 035205 (2017).

[40] Z. Li, A. Tudi, P. Ren, Y. Yang, T. Iitaka, T. Tohyama, Z. Yang, S. Pan, and H. Su, $NaPN_2$: Deep-ultraviolet nonlinear optical material with unprecedented strong second-harmonic generation coefficient, Phys. Rev. Mater. **3**, 025201 (2019).

[41] R. S. Jacobsen, K. N. Andersen, P. I. Borel, J. Fage-Pedersen, L. H. Frandsen, O. Hansen, M. Kristensen, A. V. Lavrinenko, G. Moulin, H. Ou, C. Peucheret, B. Zsigri, and A. Bjarklev, Strained silicon as a new electro-optic material, Nature (London) **441**, 199 (2006).

[42] T. D. Boyko, A. Hunt, A. Zerr, and A. Moewes, Electronic Structure of Spinel-Type Nitride Compounds Si_3N_4, Ge_3N_4, and Sn_3N_4 With Tunable Band Gaps: Application to Light Emitting Diodes, Phys. Rev. Lett. **111**, 097402 (2013).

[43] B. Zabelich, E. Nitiss, A. Stroganov, and C.-S. Bres, Linear electro-optic effect in silicon nitride waveguides enabled by electric-field poling, ACS Photonics **9**, 3374 (2022).

[44] H. L. He, T. Sekine, T. Kobayashi, H. Hirosaki, and I. Suzuki, Shock-induced phase transition of β-Si_3N_4 and c-Si_3N_4, Phys. Rev. B **62**, 11412 (2000).

[45] T. D. Boyko, E. Bailey, A. Moewes, and P. F. McMillan, Class of tunable wide band gap semiconductors γ-$(Ge_xSi_{1-x})_3N_4$, Phys. Rev. B **81**, 155207 (2010).

[46] M. Schwarz, G. Miehe, A. Zerr, E. Kroke, B. T. Poe, H. Fuess, and R. Riedel, Spinel-Si_3N_4: Multi-anvil press synthesis and structural refinement, Adv. Mater. **12**, 883 (2000).

[47] J. P. Perdew, K. Burke, and M. Ernzerhof, Generalized Gradient Approximation Made Simple, Phys. Rev. Lett. **77**, 3865 (1996).

[48] G. Kresse and J. Furthmuller, Efficiency of ab-initio total energy calculations for metals and semiconductors using a plane-wave basis set, Com. Mater. Sci. **6**, 15 (1996).

[49] See Supplemental Material at http://link.aps.org/supplemental/10.1103/PhysRevB.107.245203 for more information about structural parameters, calculated band structures, and optical properties.

[50] A. P. Jaroenjittichai and W. R. L. Lambrecht, Electronic band structure of Mg-IV-N_2 compounds in the quasiparticle-self-consistent *GW* approximation, Phys. Rev. B **94**, 125201 (2016).

[51] R. J. Bruls, H. T. Hintzen, R. Metselaar, and C. K. Loong, Anisotropic thermal expansion of $MgSiN_2$ from 10 to 300 K as measured by neutron diffraction, J. Phys. Chem. Solids **61**, 1285 (2000).

[52] Z. A. Gál, P. M. Mallinson, H. J. Orchard, and S. J. Clarke, Synthesis and structure of alkaline earth silicon nitrides: $BaSiN_2$, $SrSiN_2$ and $CaSiN_2$, Inorg. Chem. **43**, 3998 (2004).

[53] E. Sjöstedt, L. Nordström, and D. J. Singh, An alternative way of linearizing the augmented plane-wave method, Solid State Commun. **114**, 15 (2000).

[54] A. Punya, W. R. L. Lambrecht, and M. van Schilfgaarde, Quasiparticle band structure of Zn-IV-N_2 compounds, Phys. Rev. B **84**, 165204 (2011).

[55] T. de Boer, T. D. Boyko, C. Braun, W. Schnick, and A. Moewes, Band gap and electronic structure of $MgSiN_2$ determined using soft X-ray spectroscopy and density functional theory, Phys. Status Solidi RRL **9**, 250 (2015).

[56] F. Tran and P. Blaha, Accurate Band Gaps of Semiconductors and Insulators with a Semilocal Exchange-Correlation Potential, Phys. Rev. Lett. **102**, 226401 (2009).

[57] L. Hedin, New method for calculating the one-particle Green's function with application to the electron-gas problem, Phys. Rev. **139**, A796 (1965).

[58] X. Gonze *et al.*, Recent developments in the ABINIT software package, Comput. Phys. Commun. **205**, 106 (2016).

[59] S. Sharma and C. Ambrosch-Draxl, Second-harmonic optical response from first principles, Phys. Scr. **T109**, 128 (2004).

[60] A. J. Mercante, D. L. K. Eng, M. Konkol, P. Yao, S. Shi, and D. W. Prather, Thin $LiNbO_3$ on insulator electro-optic modulator, Opt. Lett. **41**, 867 (2016).

[61] Y.-J. Hyun, J.-Y. Choi, and S.-K. Han, Dual polarization simultaneous optical intensity modulation in single birefringent $LiNbO_3$ Mach-Zehnder optical modulator, Photonics **9**, 386 (2022).